Mon. Not. R. Astron. Soc. **361,** 1250–1256 (2005) doi:10.1111/j.1365-2966.2005.09257.x

Strong gravitational lensing and dynamical dark energy

Andrea V. Macciò[1,2,3]★

[1]*Institute for Theoretical Physics, University of Zürich, CH-8057 Zürich, Switzerland*
[2]*Physics Department G. Occhialini, Università degli Studi di Milano–Bicocca, Piazza della Scienza 3, I-20126 Milan, Italy*
[3]*INFN, via Celoria 16, I-20133 Milan, Italy*

Accepted 2005 June 2. Received 2005 May 9; in original form 2004 March 2

ABSTRACT

We study the strong gravitational lensing properties of galaxy clusters obtained from *N*-body simulations with different kinds of dark energy (DE). We consider both dynamical DE, due to a scalar field self-interacting through Ratra–Peebles (RP) or supergravity (SUGRA) potentials, and DE with constant negative $w = p/\rho = -1$ (ΛCDM). We have 12 high-resolution lensing systems for each cosmological model with mass greater than $5.0 \times 10^{14}\, h^{-1}\, \mathrm{M}_{\odot}$. Using a ray shooting technique, we make a detailed analysis of the lensing properties of these clusters, paying particular attention to the number of arcs and their properties (magnification, length and width). We find that the number of giant arcs produced by galaxy clusters changes in a considerable way from ΛCDM models to dynamical dark energy models with an RP or SUGRA potential. These differences originate from the different epochs of cluster formation and from the non-linearity of the strong lensing effect. We suggest that strong lensing is one of the best tools to discriminate among different kinds of dark energy.

Key words: methods: analytical – methods: numerical – galaxies: clusters: general – galaxies: haloes – cosmology: theory – dark matter.

1 INTRODUCTION

The mounting observational evidence for the existence of dark energy (DE), which probably accounts for ∼70 per cent of the critical density of the Universe (Riess et al. 1998; Perlmutter et al. 1999; Tegmark, Zaldarriaga & Hamilton 2001; Netterfield et al. 2002; Efstathiou et al. 2002; Percival et al. 2002; Pogosian, Bond & Contaldi 2003; Spergel et al. 2003), raises a number of questions concerning galaxy formation. The nature of DE is suitably described by the parameter $w = p/\rho$, which characterizes its equation of state. The ΛCDM model ($w = -1$) has been extensively studied during the past decade. Recently, much more attention has been given to physically motivated models with variable w Mainini, Macciò & Bonometto (2003a), for which a number of *N*-body simulations have been performed (Klypin et al. 2003, hereafter KMMB03; Dolag et al. 2004; Linder & Jenkins 2003; Macciò et al. 2004). One of the main results of KMMB03 was that dynamical DE haloes are denser than those with the standard ΛCDM one. In this work we want to analyse the impact of this higher concentration on the strong lensing properties of the cluster size haloes.

It was first noted by Bartelmann et al. (1998) (for OCDM, SCDM and ΛCDM cosmologies) that the predicted number of giant arcs varies by orders of magnitude among various cosmological models. The agreement between data and ΛCDM simulations has been tested by many authors (see Meneghetti et al. 2000; Dalal, Holder & Hennawi 2004; Wambsganss et al. 2004), but the situation is still unclear. A direct comparison of arc statistics with observational data is beyond the scope of this work. What we want to point out here is the capability of strong lensing to discriminate between different kinds of dark energy [a similar paper, but for a different choice of the dynamical DE parameters, was recently submitted by Meneghetti et al. (2005)].

Here, using a ray shooting technique, we make a lensing analysis of dark matter haloes extracted from *N*-body simulations of cosmological models with varying w arising from physically motivated potentials that admit tracker solutions. In particular, we focus on the two most popular variants of dynamical DE (Ratra & Peebles 1988; Wetterich 1988, 1995). The first model was proposed by Ratra & Peebles (1984, hereafter RP) and it yields a rather slow evolution of w. The second model (Brax & Martin 1999, 2000; Brax, Martin & Riazuelo 2000) is based on potentials found in supergravity (SUGRA) and it results in a much faster evolving w. Hence, RP and SUGRA potentials cover a large spectrum of evolving w. These potentials are written as

$$V(\phi) = \frac{\Lambda^{4+\alpha}}{\phi^{\alpha}} \qquad \text{RP}, \tag{1}$$

$$V(\phi) = \frac{\Lambda^{4+\alpha}}{\phi^{\alpha}}\, \exp(4\pi G\phi^2) \qquad \text{SUGRA}. \tag{2}$$

Here Λ is an energy scale, currently set in the range 10^2–10^{10} GeV, relevant for the physics of fundamental interactions. The potentials

★E-mail: andrea@pegasus.physik.unizh.ch

depend also on the exponent α. The parameters Λ and α define the DE density parameter $\Omega_{\rm DE}$. However, we prefer to use Λ and $\Omega_{\rm DE}$ as independent parameters. Fig. 10 in Mainini et al. (2003b) gives examples of w evolution for RP and SUGRA models.

The SUGRA model considered in this paper has $\Lambda = 10^3$ GeV, which implies $w = -0.85$ at $z = 0$, but w drastically changes with redshift: $w \approx -0.4$ at $z = 5$. The first RP model ($\rm RP_1$) has the same value for Λ as the SUGRA model. At redshift $z = 0$ it has $w = -0.5$; then the value of w gradually changes with redshift: at $z = 5$ it is close to -0.4. Although the w interval spanned by this RP model covers values significantly above -0.8 (not favoured by observations), this case is still important both as a limiting reference case and to emphasize that models with constant w and models with variable w produce different results even if the average values of w are not so different. For the second RP model ($\rm RP_2$), we have chosen $\Lambda = 10^{-8}$ GeV; in this case the value of the state parameter at redshift $z = 0$ is the same as SUGRA: $w(z = 0, \Lambda = 10^{-8}\ \text{GeV}) = -0.85$. This model is certainly in better agreement with cosmic microwave background (CMB) constraints, but it loses most of its interest from a theoretical point of view: such a small value of Λ has no clear connection with the physics of fundamental interactions, and so it has exactly the same 'fine tuning' problem as the ΛCDM model.

We have normalized all the models in order to have today the same value of the rms density fluctuation on a scale of $8\,h^{-1}$ Mpc, which has been chosen as $\sigma_8 = 0.8$.

2 *N*-BODY SIMULATIONS

The adaptive refinement tree code ART (Kravtsov, Klypin & Khokhlov 1997) was used to run the simulations. The ART code starts with a uniform grid, which covers the whole computational box. This grid defines the lowest (zeroth) level of resolution of the simulation. The standard particles–mesh algorithms are used to compute density and gravitational potential on the zeroth-level mesh. The ART code reaches high force resolution by refining all high-density regions using an automated refinement algorithm. The refinements are recursive: the refined regions can also be refined, each subsequent refinement having half of the previous level's cell size. This creates a hierarchy of refinement meshes of different resolution, size and geometry covering regions of interest. Because each individual cubic cell can be refined, the shape of the refinement mesh can be arbitrary and match effectively the geometry of the region of interest.

The criterion for refinement is the local density of particles: if the number of particles in a mesh cell (as estimated by the cloud-in-cell method) exceeds the level $n_{\rm thresh}$, the cell is split ('refined') into eight cells of the next refinement level. The refinement threshold depends on the refinement level. For the zero level it is $n_{\rm thresh} = 2$. For the higher levels it is set to $n_{\rm thresh} = 4$. The code uses the expansion parameter a as the time variable. During the integration, spatial refinement is accompanied by temporal refinement. Namely, each level of refinement, l, is integrated with its own time-step $\Delta a_l = \Delta a_0/2^l$, where $\Delta a_0 = 3 \times 10^{-3}$ is the global time-step of the zeroth refinement level. This variable time-stepping is very important for the accuracy of the results. As the force resolution increases, more steps are needed to integrate the trajectories accurately. Extensive tests of the code and comparisons with other numerical N-body codes can be found in Kravtsov et al. (1997) and Knebe et al. (2000). The code was modified to handle DE of different types (Mainini et al. 2003b; KMMB03).

We performed a low-resolution simulation for each model with the following parameters: box size, 320 h^{-1} Mpc; number of particles, 128^3; force resolution, $9.2\,h^{-1}$ kpc. All the simulations have the same initial random seed so at $z = 0$ the clusters are more or less in the same positions. Then we selected the four massive clusters in the ΛCDM simulation and re-ran them with a mass resolution 64 times higher. The same clusters are also re-run with the same resolution also in the RP and SUGRA models. At the end we have 12 lensing systems (each cluster can be seen by three different orthogonal directions) for each cosmological model, with a mass resolution of $2.03 \times 10^{10}\,h^{-1}\,\rm M_\odot$ and a force resolution of $4.8\,h^{-1}$ kpc. A complete list of simulation parameters is contained in Table 1.

Table 1. Parameters of simulations.

Model	Λ (GeV)	Box (h^{-1} Mpc)	$N_{\rm p}$	$M_{\rm res}$ ($h^{-1}\,\rm M_\odot$)	$F_{\rm res}$ (h^{-1} kpc)
$\rm RP_1$	10^3	320	512^3	2.03×10^{10}	4.8
$\rm RP_2$	10^{-8}	320	512^3	2.03×10^{10}	4.8
SUGRA	10^3	320	512^3	2.03×10^{10}	4.8
ΛCDM	0	320	512^3	2.03×10^{10}	4.8

3 LENSING SIMULATIONS

In order to compute arc statistics for the models discussed above, we adopted a technique similar to the one originally proposed by Bartelmann & Weiss (1994). We centre the cluster in a cube of $4\,h^{-1}$ Mpc side length and study three lenses, obtained by projecting the particle positions along the coordinate axes. This grants us a total of 12 lens planes per model that we treat as though being due to independent clusters, for our present purposes.

We then divide the projected density field Σ by the critical surface mass density for lensing

$$\Sigma_{\rm cr} = \frac{c^2}{4\pi G}\frac{D_{\rm S}}{D_{\rm L} D_{\rm LS}}, \tag{3}$$

so obtaining the convergence k. Here c is the speed of light, G is the gravitational constant, while $D_{\rm L}$, $D_{\rm S}$ and $D_{\rm LS}$ are the angular-diameter distances between lens and observer, source and observer, and lens and source, respectively. Once we set the lens and source redshifts, the value of the angular-diameter distance depends on the cosmological model. We detail this point in the next section. In Fig. 1 we show the convergence map for one of the clusters, whose length-scale size is $4\,h^{-1}$ Mpc. The deflection angle due to this 2D particle distribution, on a given point $\boldsymbol{x}$ on the lens plane, reads

$$\boldsymbol{\alpha}(\boldsymbol{x}) = \sum_{j=1}^{N} \frac{4G}{c^2}\frac{m_j}{|\boldsymbol{x} - \boldsymbol{y}_j|}. \tag{4}$$

Here $\boldsymbol{y}_j$ is the position of the jth particle and N is the total number of particles.

As direct summation requires a long time, we speed up the code by using a $\rm P^3M$-like algorithm: the lens plane was divided into 128×128 cells and direct summation was applied to particles belonging to the same cell of $\boldsymbol{x}$ and for its eight neighbouring cells. Particles in other cells were then seen as a single particle in the cell baricentre, given the total mass of the particles inside the cell.

The deflection angle diverges when the distance between a light ray and a particle is zero. To avoid this unwanted feature, we introduce a softening parameter ϵ in equation (4); the value ϵ is tuned on the resolution of the current simulation.

We start to compute $\boldsymbol{\alpha}(\boldsymbol{x})$ on a regular grid of 256×256 test rays that covered the central quarter of the lens plane, then we propagate

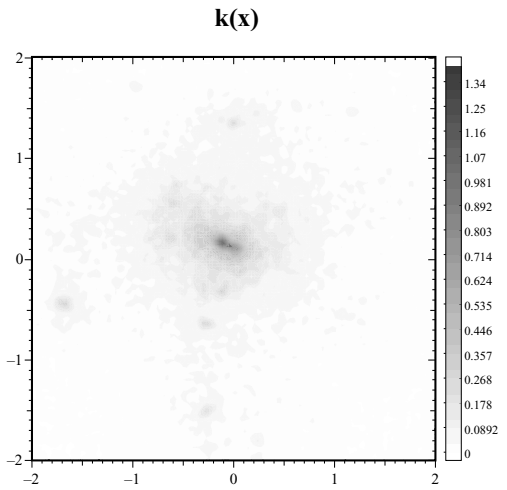

Figure 1. Convergence map for one of the ΛCDM clusters. The side length is $4\,h^{-1}$ Mpc. In the central part, $k > 1$, so this halo is able to produce giant arcs.

a bundle of 2048 × 2048 light rays and determine the deflection angle on each light ray by bicubic interpolation amongst the four nearest test rays (see Section 3.2 for further discussion on the effects of the adopted resolution in the lens mapping).

The relation between images and source positions is given by the lens equation:

$$\boldsymbol{y} = \boldsymbol{x} - \boldsymbol{\alpha}(\boldsymbol{x}), \tag{5}$$

and the local properties of the lens mapping are then described by the Jacobian matrix of the lens equation,

$$A_{hk}(\boldsymbol{x}) = \frac{\partial y_h}{\partial x_k} = \delta_{hk} - \frac{\partial \alpha_h}{\partial x_k}. \tag{6}$$

The shear components γ_1 and γ_2 are found from A_{hk} through the standard relations

$$\gamma_1(\boldsymbol{x}) = -\tfrac{1}{2}[A_{11}(\boldsymbol{x}) - A_{22}(\boldsymbol{x})], \tag{7}$$

$$\gamma_2(\boldsymbol{x}) = -\tfrac{1}{2}[A_{12}(\boldsymbol{x}) + A_{21}(\boldsymbol{x})], \tag{8}$$

and the magnification factor μ is given by the Jacobian determinant,

$$\mu(\boldsymbol{x}) = \frac{1}{\det A} = [A_{11}(\boldsymbol{x})A_{22}(\boldsymbol{x}) - A_{12}(\boldsymbol{x})A_{21}(\boldsymbol{x})]^{-1}. \tag{9}$$

Finally, the Jacobian determines the location of the critical curves $\boldsymbol{x}_{\rm c}$ on the lens plane, which are defined by $\det A(\boldsymbol{x}_{\rm c}) = 0$. Because of the finite grid resolution, we can only approximately locate them by looking for pairs of adjacent cells with opposite signs of $\det A$. Then, the lens equations

$$\boldsymbol{y}_{\rm c} = \boldsymbol{x}_{\rm c} - \boldsymbol{\alpha}(\boldsymbol{x}_{\rm c}) \tag{10}$$

yield the corresponding caustics $\boldsymbol{y}_{\rm c}$ on the source plane.

3.1 Deformation of sources

For statistical purposes, one has to distribute and map a large number of sources. We are interested in arc properties and arcs form near caustics; so for numerical efficiency we have to distribute less sources in those parts of the source plane that are far away from any caustics, and more sources close to or inside the caustics. We follow the method introduced by Miralda-Escudè (1993) and later adapted to non-analytical models by Bartelmann & Weiss (1994). In the previous section we have obtained the deflection angles for the $\boldsymbol{x}_{ij}$ (with $i, j = 1, \ldots, 2048$) positions on the lens (or image) plane. Using the lens equation (10) we can obtain the corresponding positions on the source plane $\boldsymbol{y}_{ij}$ ($\boldsymbol{x}_{ij}$). As usual, we call this discrete transformation the *mapping table*.

We model elliptical sources with axial ratios randomly drawn from the interval [0.5;1] and area equal to that of a circle with radius $r_{\rm s} = 0.5$ arcsec. We first distribute sources on a coarse grid of 32×32, defined in the central quarter of the source plane covered by the light rays traced (as a result of convergence, only a restricted part of the source plane can be reached by the light rays traced from the observer through the lens plane). From the mapping table, we obtain the magnification μ. If it changes by more than one (absolute value) between two sources, we place an additional source between the two. In this way we increase the resolution by a factor of 2 in each dimension. For the nth iteration of source positions, the criterion to add additional sources is that magnification changes by 2^{n-1}. We repeat this procedure four times to obtain the final list of source positions. To compensate for this artificial increase in the source number density, we assign a statistical weight of 2^{1-n} to each image of a source placed during the nth grid refinement. On average we have about 15 000 sources for each lensing system.

3.2 Analysis of arcs

To find the images of an extended source, all image plane positions $\boldsymbol{x}$ are checked if the corresponding entry in the mapping table $\boldsymbol{y}$ lies within the source: i.e. for an elliptical source with axes a, b and centred on $(y_1^{\rm c}; y_2^{\rm c})$, it is checked if

$$\frac{\left(y_1 - y_1^{\rm c}\right)^2}{a^2} + \frac{\left(y_2 - y_2^{\rm c}\right)^2}{b^2} \leqslant 1, \tag{11}$$

where (y_1, y_2) are the components of the vector $\boldsymbol{y}$.

Those points fulfilling the previous equation are part of one of the source images and are called image points. We then use a standard *friends-of-friends* algorithm to group together image points within connected regions, since they belong to the same image (the number of images of one source ranges from 1 to 5 for our clusters).

We measure arc properties using a method based on Bartelmann & Weiss (1994). The arc area and magnification are found by summing the areas of the pixel falling into the image. Arc lengths are estimated by first finding the arc centre, then finding the arc pixel farthest from the centroid as well as the pixel farthest from this pixel. The arc length is then given by the sum of the lengths of the two lines connecting these three points. The arc width is defined as the ratio between the arc area and the arc length.

In Fig. 2 we plot the relation between length/width ratio and magnification; we found a good agreement with previous results obtained by Dalal et al. (2004). The scatter in this relation is due to local fluctuations in the surface mass density. Highly distorted images are also highly magnified, but the converse is not always true.

Before proceeding with our analysis, we performed some tests on the resolution adopted in our ray shooting code. Fig. 3 shows the fraction of sources (number of sources divided by the total number) versus their length/width ratio for different values of the resolution of the lens mapping grid $N_{\rm hr}^2$ (results are for the ΛCDM model with $z_{\rm l} = 0.3$ and $z_{\rm s} = 1.0$). If the resolution of the lens mapping is not high enough, the critical curves are too small compared to the source size and a spurious cut-off in the number of arcs with $L/W > 10$

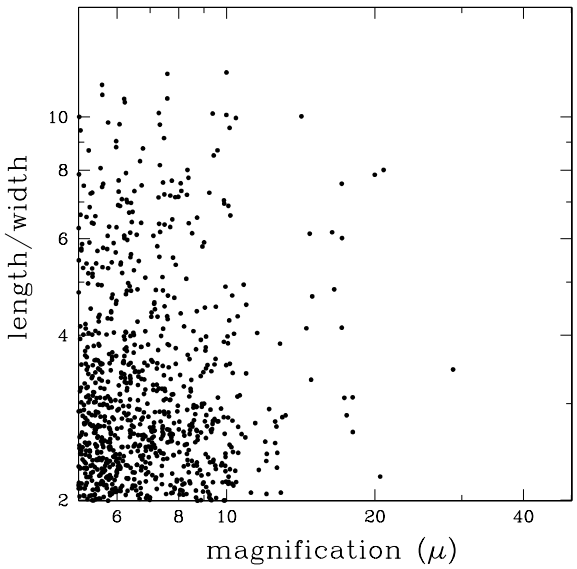

Figure 2. Magnification versus length/width ratio for ΛCDM clusters. These two quantities are equal for an isothermal sphere lens.

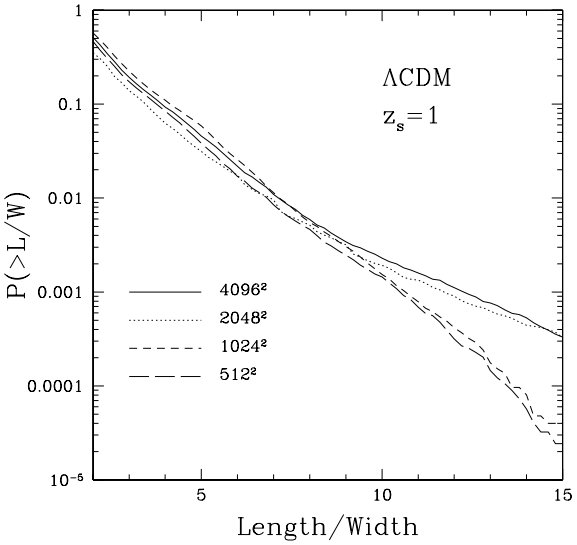

Figure 3. Fraction of sources mapped in an arc versus length/width ratio of the arc for different values of the resolution of the lensing mapping. All curves are for the ΛCDM model with $z_l = 1.0$ and $z_s = 0.3$.

appears. This cut-off is totally artificial and it vanishes for $N_{hr} \geqslant 2048$. As Fig. 3 shows, the results are stable also for a higher value of N_{hr} (4096). Then in order to have a good compromise between resolution and computational time, we have adopted $N_{hr} = 2048$ in the following.

4 ARC STATISTICS

In this paper we aim to compare the lensing properties of a given cluster as it appears in different cosmological models. There are three main features that affect the number of giant arcs: the concentration of the halo, the total number of lensing systems at a given redshift, and the value of the critical surface mass density (Σ_{cr}).

As predicted analytically by Bartelmann, Perrotta & Baccigalupi (2002) (for constant w models) and first noted in numerical N-body

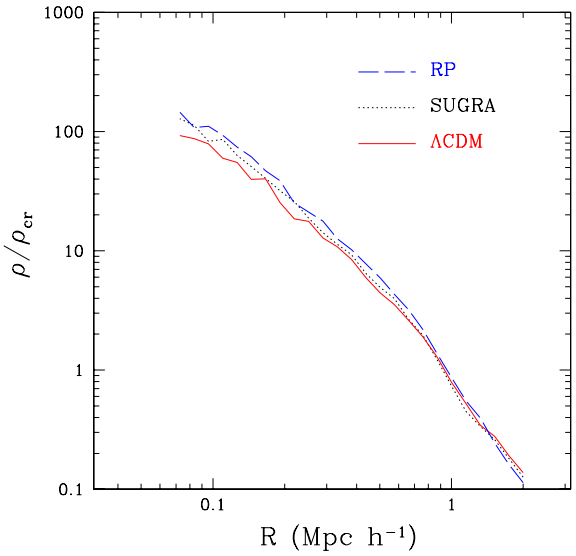

Figure 4. Density profile of the same halo simulated in different models. The full (red online) curve is for ΛCDM, the dotted (black) one for SUGRA, and the dashed (blue) one for RP_1. The halo has a virial mass of $6 \times 10^{14}\, h^{-1}\, M_\odot$.

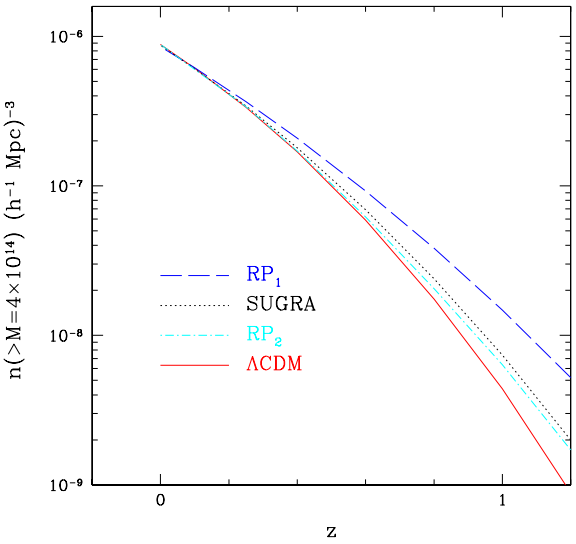

Figure 5. Number density of haloes with mass greater than $4.0 \times 10^{14}\, h^{-1}\, M_\odot$ for ΛCDM [solid (red online) curve], SUGRA [dotted (black) curve] and the two RP models, RP_1 [dashed (blue) curve] and RP_2 [dot-dashed (cyan) curve]. The value of Λ is 10^3 GeV for both RP_1 and SUGRA, and 10^{-8} GeV for RP_2.

simulations by KMMB03, and then confirmed by Dolag et al. (2004) and Linder & Jenkins (2003), the concentration of dynamical DE haloes is greater than the concentration of ΛCDM ones. Here we use the same definition of concentration as KMMB03: the ratio of the radius at the overdensity of the ΛCDM model (103 times the critical density) to the characteristic ('core') radius of the Navarro, Frenk & White (NFW) profile (see however KMMB03 for more details). A greater concentration increases the probability of forming giant arcs. In Fig. 4 we report the density profile of the same halo simulated in different cosmological models. The RP_1 halo is clearly denser and more concentrated than the ΛCDM halo, with the SUGRA

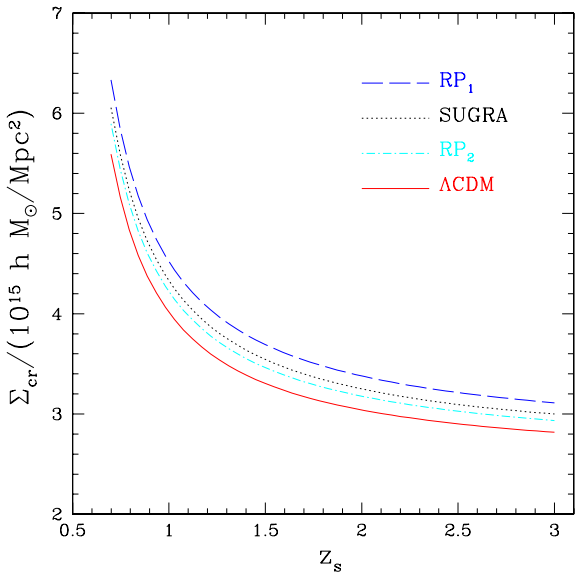

Figure 6. Value of the critical surface mass density $\Sigma_{\rm cr}$ in different cosmological models (curves as for Fig. 5). For all the curves we choose a lens redshift $z_l = 0.4$.

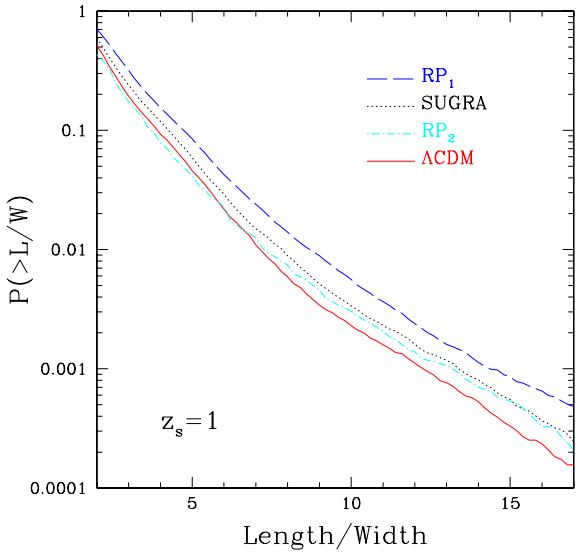

Figure 7. Fraction of sources mapped in an arc versus length/width ratio of the arc. The uppermost curve is RP_1 (dashed, blue online); then from top to bottom we have SUGRA (dotted, black), RP_2 (dot-dashed, cyan) and ΛCDM (full, red) results.

halo laying in between; the RP_2 halo (which is not shown in this plot) has a concentration parameter close to the one of the ΛCDM model.

The expected number of objects with mass exceeding $4 \times 10^{14}\,h^{-1}\,{\rm M}_\odot$ (in order to produce multiple images) at a given redshift (in this case $z = 0.4$) can be estimated using a Press–Schechter formalism (see Mainini et al. 2003a). In dynamical DE, objects form earlier than in ΛCDM, so we have more lensing systems per $\rm Mpc^3$ at $z = 0.3$. This can be taken into account by multiplying the number of arcs by 1.3, 1.21 and 1.12 in RP_1, SUGRA and RP_2, respectively. (In Fig. 5 we report the evolution with redshift of the mass function for a mass threshold of $4.0 \times 10^{14}\,h^{-1}\,{\rm M}_\odot$.)

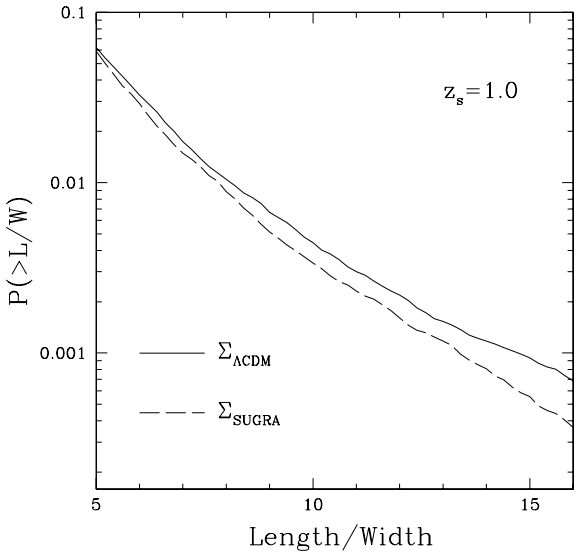

Figure 8. Same plot as Fig. 7 for the SUGRA model where the arc properties are computed using $\Sigma_{\rm cr}$(ΛCDM) (solid line) and $\Sigma_{\rm cr}$(SUGRA) (dashed line).

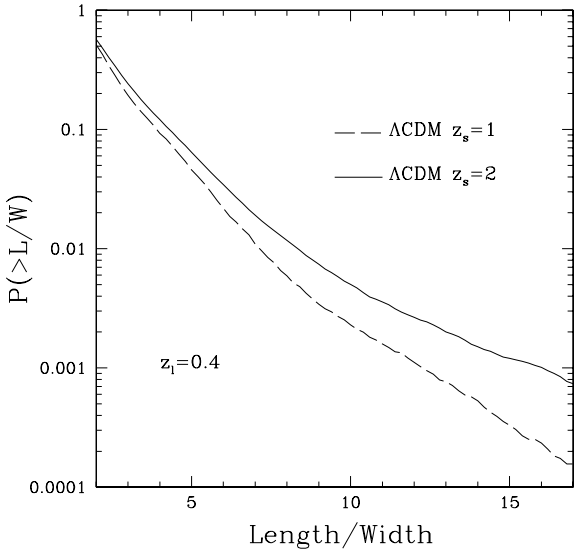

Figure 9. Arc counts for two different values of the source redshift in the ΛCDM model.

The evolution of the scalefactor a with time also depends on the model. This implies that, at a given redshift $z = 1/a - 1$, the angular-diameter distance $D_{\rm ad}$ is model-dependent; in fact its value is given by

$$D_{\rm ad}(a) = \frac{ac}{H_0} \int_a^1 \sqrt{\frac{a[1-\Omega_{\rm DE}(a)]}{\Omega_{\rm m,0}}}\,{\rm d}a. \qquad (12)$$

Here c is the speed of light, H_0 and $\Omega_{\rm m,0}$ are the present value of the Hubble constant and the matter density parameter, and $\Omega_{\rm DE}\,(a)$ gives the evolution of the DE density parameter with the expansion factor. To compute $\Omega_{\rm DE}(a)$ for RP and SUGRA models, we have used the analytical expression of Mainini et al. (2003b). In Fig. 6 we show the value of the critical surface mass density for the adopted cosmological models. The different values for $\Sigma_{\rm cr}$ mean that a ΛCDM halo yields more arcs than a dynamical DE halo, if they have the

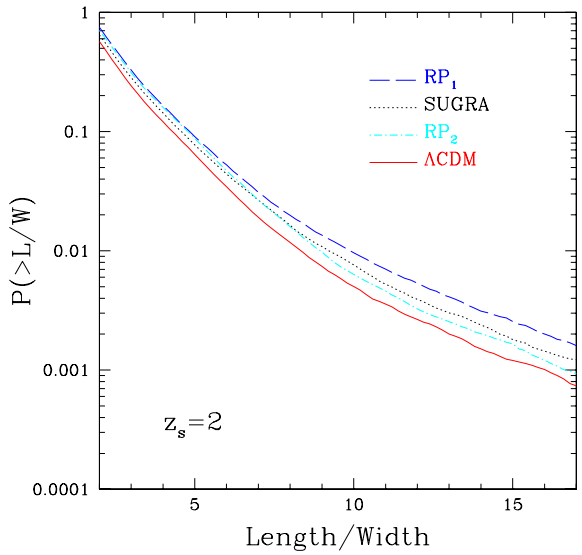

Figure 10. The same as Fig. 7 for $z_s = 2$. With this value for the source redshift, the number of arcs increases in all the models.

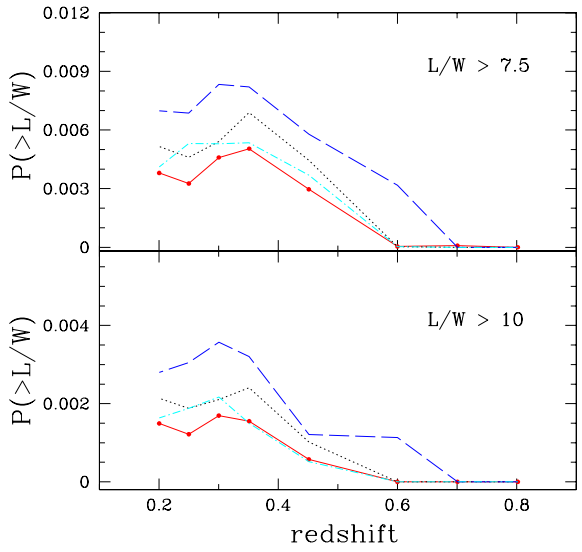

Figure 11. Number of arcs versus the lens redshift for two different thresholds of the L/W ratio: 10 and 7.5. Solid (red online) line is for ΛCDM, dashed (blue) for RP_1, dot-dashed (cyan) for RP_2, and dotted (black) for SUGRA ($z_s = 1.0$).

same surface mass density. The effect of the different values of the angular-diameter distance tends therefore to reduce the number of arcs in dynamical DE models.

The first result of our analysis is shown in Fig. 7, where we plot the fraction of sources (number of sources divided by the total number) versus their length/width ratio for a cluster (lens) redshift $z_l = 0.3$, where lensing is most efficient for a source redshift of 1.0 (as shown later in Fig. 11). As expected, the RP_1 model produces more distorted images, due to its more concentrated haloes. The SUGRA and RP_2 models are quite similar for $L/W > 10$ and they lay in between RP_1 and ΛCDM, which, as expected, produces less highly distorted images than the dynamical DE models. We want to underline that part of the higher lensing signal due to the higher concentration of dark matter haloes in such models is cancelled by the increased Σ_{cr} value. This effect is clearly illustrated in Fig. 8, where we have computed the arc statistics in a SUGRA model using the ΛCDM critical surface density. As expected, we have obtained a result for SUGRA that is closer to the RP_1 one.

As pointed out by many authors (Wambsganss, Bode & Ostriker 2004; Dalal et al. 2004), the number of arcs that a cluster is able to produce is strongly related to the redshift of the sources (although the strength of this effect is not yet completely understood, various authors having found different results). In Fig. 9 we plot the arc number counts for the ΛCDM model for $z_s = 1$ (dashed line) and $z_s = 2$ (solid line). As in previous work we found that the number of arcs increases if we increase the source redshifts. Fig. 10 shows the same results of Fig. 7, but for $z_s = 2$.

As expected, the total number of arcs increases in all cosmological models. Again we have a sort of hierarchy of results according to what is expected from the dynamical evolution of dark matter haloes in the corresponding cosmological model.

Moreover, owing to the lower difference in the value of Σ_{cr} for this source redshift, the four models are better separated, especially the SUGRA and RP_2 ones. A difference between these two models is somewhat expected even if they have the same value of state parameter today ($w = -0.84$). This arises from the different evolution of w: in SUGRA it drastically changes with redshift ($w = -0.4$ at $z = 5$), whereas it is more constant in RP_2 ($w = -0.72$ at $z = 5$).

As the final result, in Fig. 11 we show the evolution with lens redshift of the number of arcs for two different choices of the length/width ratio: 10 and 7.5 (the redshift of the sources is $z_s = 1.0$). On average the RP_1 model is always above the others; instead, the difference between SUGRA and ΛCDM is more or less constant at all redshifts and the lensing signal decreases rapidly for $z > 0.45$.

The RP_2 model has a sort of double behaviour: it is close to ΛCDM for $z > 0.35$ but it is more similar to SUGRA for $z < 0.35$. We think that this bimodality is again due to the evolution of the state parameter in this model, especially if compared to the SUGRA one. The ratio w_{RP_2}/w_{SU} decreases with redshift towards unity at $z = 0$, so it is less different from ΛCDM at high redshift in respect to SUGRA.

The peaks in the lensing signal have slightly different positions in the different models. As argued by other authors (Torri et al. 2004), this could be due to time offset between merger events in different dark energy cosmologies.

5 DISCUSSION AND CONCLUSIONS

Models with dynamical DE are in an infant state. We do not know the nature of DE. Thus, the state parameter $w(t)$ is still uncertain. In view of this functional indeterminacy, at first sight it could seem that the situation is hopeless.

In spite of that, we can outline some general trends that result from our analysis. In dynamical DE models, haloes tend to collapse earlier than in a ΛCDM model with the same normalization at $z = 0$. As the result, haloes are more concentrated and denser in their inner parts (KMMB03). Starting from this finding, we have explored the consequences of this higher concentration on the strong lensing properties of dark matter haloes, in SUGRA and RP cosmologies.

We found that RP_1 haloes (obtained assuming the cluster abundance of the power spectrum and a value for the energy scale Λ in the range suggested by the physics of fundamental interactions) produce a higher number of arcs with a $L/W > 10$ if compared to the standard ΛCDM model. This model (RP_1) is marginally consistent with the observations and its purpose is mainly to illustrate the

principal effect of a dynamical dark energy component on the arcs statistic.

The second model we analysed based on RP potential (RP_2) is more realistic from an observational point of view but less motivated by theoretical arguments. This model produces about 50 per cent more arcs with $L/W > 10$ than the ΛCDM one for $z_l = 0.3$ and $z_s = 1$, but it is marginally distinguishable from ΛCDM for lensing systems at moderately high redshift ($z_l > 0.35$, Fig. 11) or for high-redshift sources/arcs ($z_l = 0.3$ and $z_s = 2$).

The SUGRA model is always in between the ΛCDM and the RP_1 models and it produces about 70–80 per cent more arcs than ΛCDM. This difference is almost constant on changing both the source and the lens redshifts, and it tends to disappear for $z_l > 0.6$ (for $z_s = 1.0$), where all the lensing systems considered in this paper ($M_1 \approx 5 \times 10^{14}$) are unable to produce highly distorted images (except in the test model RP_1). We also noted that part of the stronger lensing signal due to the higher concentration of haloes in dynamical DE models is partially cancelled by geometrical effects that increase the critical surface density in such models (Figs 6 and 8).

As a final remark we would like to stress that the arc statistic is a powerful tool to investigate the nature of dark energy. The forthcoming observational surveys (i.e. CFHT Legacy Survey, SDSS and others) will improve the statistics of giant arcs on the sky [for example, the RCS-2 Survey (Gladders et al. 2003) will cover an area of 830 $\deg^2$ and is expected to produce 50–100 new arcs]. Such observational material will provide a discrimination between DE cosmologies, possibly allowing one to constrain the Λ scale of the SUGRA and RP potentials.

ACKNOWLEDGMENTS

It is a pleasure to thank Massimo Meneghetti for his help and his comments on lensing simulations and Roberto Mainini for useful discussions on dynamical dark energy models. We also thank Silvio Bonometto and Ben Moore for carefully reading the manuscript and INAF for allowing us to use the computer resources at the CINECA Consortium (grant cnami44a on the SGI Origin 3800 machine).

REFERENCES

Bartelmann M., Weiss A., 1994, A&A, 287, 1
Bartelmann M., Huss A., Carlberg J., Jenkins A., Pearce F., 1998, A&A, 330, 1
Bartelmann M., Perrotta F., Baccigalupi C., 2002, A&A, 396, 21
Brax P., Martin J., 1999, Phys. Lett. B, 468, 40
Brax P., Martin J., 2000, Phys. Rev. D, 61, 103502
Brax P., Martin J., Riazuelo A., 2000, Phys. Rev. D, 62, 103505
Dalal N., Holder G., Hennawi J. F., 2004, AJ, 609, 50
Dolag K., Bartelmann M., Perrotta F., Baccigalupi C., Moschardini L., Meneghetti M., Tormen G., 2004, A&A, 416, 853
Efstathiou G. et al., 2002, MNRAS, 330, L29
Gladders M. D., Hoekstra H., Yee H. K. C., Hall P. B., Barrientos L. F., 2003, ApJ, 593, 48
Klypin A., Macciò A. V., Mainini R., Bonometto S. A., 2003, ApJ, 599, 31 (KMMB03)
Knebe A., Kravtsov A., Gottlober S., Klypin A., 2000, MNRAS, 317, 630
Kravtsov A., Klypin A., Khokhlov A., 1997, ApJ, 111, 73
Linder E., Jenkins A., 2003, MNRAS, 346, 573
Luppino G. A., Gioia I. M., Hammer F., Le Fevre O., Annis J. A., 1999, A&AS, 136, 117
Macciò A. V., Quercellini C., Mainini R., Amendola L., Bonometto S. A., 2004, Phys. Rev. D, 69, 123516
Mainini R., Macciò A. V., Bonometto S. A., 2003a, New Astron., 8, 172
Mainini R., Macciò A. V., Bonometto S. A., Klypin A., 2003b, ApJ, 599, 24
Meneghetti M., Bolzonella M., Bartelmann M., Moscardini L., Tormen G., 2000, MNRAS, 314, 338
Meneghetti M., Bartelmann M., Dolag K., Moschardini L., Perrotta F., Baccigalupi C., Tormen G., 2005, New Astron. Rev., 49, 111
Miralda-Escudè J., 1993, ApJ, 403, 497
Navarro J. F., Frenk C. S., White S. D. M., 1997, ApJ, 490, 493
Netterfield C. B. et al., 2002, ApJ, 571, 604
Percival W. J. et al., 2002, MNRAS, 337, 1068
Perlmutter S. et al., 1999, ApJ, 517, 565
Pogosian D., Bond J. R., Contaldi C., 2005, in Proc. XVIII IAP Colloq., On the Nature of Dark Energy. IAP, Paris, in press (astro-ph/0301310)
Ratra B., Peebles P. J. E., 1988, Phys. Rev. D, 37, 3406 (RP)
Riess A. G. et al., 1998, AJ, 116, 1009
Spergel et al., 2003, ApJS, 148, 175
Tegmark M., Zaldarriaga M., Hamilton A. J., 2001, Phys. Rev. D, 63, 43007
Torri E., Meneghetti M., Bartelamann M., Moscardini L., Rasia E., Tormen G., 2004, MNRAS, 349, 476
Wambsganss J., Bode P., Ostriker J. P., 2004, ApJ, 606, L93
Wetterich C., 1988, Nucl. Phys. B, 302, 668
Wetterich C., 1995, A&A, 301, 32

This paper has been typeset from a TEX/LATEX file prepared by the author.